Fingerprints of transverse and longitudinal coupling between induced open quantum dots in the longitudinal magnetoconductance through antidot lattices

Sebastian Ujevic* and Michel Mendoza
Centro de Ciências Naturais e Humanas, Universidade Federal do ABC, 09210-170 Santo André, SP, Brazil
(Received 17 May 2010; revised manuscript received 5 July 2010; published 21 July 2010)

We propose numerical simulations of longitudinal magnetoconductance through a finite antidot lattice located inside an open quantum dot with a magnetic field applied perpendicular to the plane. The system is connected to reservoirs using quantum point contacts. We discuss the relationship between the longitudinal magnetoconductance and the generation of transversal couplings between the induced open quantum dots in the system. The system presents longitudinal magnetoconductance maps with crossovers (between transversal bands) and closings (longitudinal decoupling) of fundamental quantum states related to the open quantum dots induced by the antidot lattice. A relationship is observed between the distribution of antidots and the formed conductance bands, allowing a systematic follow up of the bands as a function of the applied magnetic field and quantum point-contact width. We observed a high conductance intensity [between n and $(n+1)$ quantum of conductance, $n=1,2,\ldots$] in the regions of crossover and closing of states. This suggests transversal couplings between the induced open quantum dots of the system that can be modulated by varying both the antidots potential and the quantum point-contact width. A new continuous channel (not expected) is induced by the variation in the contact width and generate Fano resonances in the conductance. These resonances can be manipulated by the applied magnetic field.

DOI: 10.1103/PhysRevB.82.035432 PACS number(s): 73.21.La, 73.63.Kv, 73.23.−b

I. INTRODUCTION

The low-dimensional systems based in two-dimensional electron gases have lead to an explosion of experimental studies of new phenomena in which the quantum wave nature of electrons plays an essential role. In the mesoscopic systems, in which the electron transport is confined to one or two dimensions, interesting effects related to the combination of fundamental constants of nature are still studied. As examples, we can mention the quantum Hall effect[1,2] and the conductance quantization.[3,4] To understand the mechanics of quantum interference that controls these effects as a function of the magnetic field,[5,6] the use of electrostatic confinement through metallics gates[7] devices as quantum wire[8,9] (QW), quantum point contacts[10,11] (QPCs), and open quantum dots[12,13] (OQDs) are adequate. In this context, the combination of electrostatic and magnetic confinement results in an elegant and useful form to manipulate the quantum interference of the electronic states.

An antidot lattice, or artificial crystal,[14,15] represents an interesting and versatile laboratory in which we may be able to induce different transport regimes by modifying the lattice characteristics and the external applied fields. The investigations in the field of magnetoelectronic transport in two-dimensional antidot lattice systems (ballistic) are mostly related to one of the following topics: (i) studies on the quantum-classical limit and its relation to quantum chaos,[16–19] which is mainly focused on the study of electrons dynamics associated with classical orbits or scars wave functions,[20–22] and (ii) studies about the manipulation of the electronic-transport regimes,[6,23–25] such as electronic localization effects, conductor-insulator transition, surface states, and quantum Hall effect. In general, these phenomena can be induced by the manipulation of quantum interference effects using different lattice geometries, shapes, sizes, and number of the antidots, or due to the intensity variation in the applied external fields.[26–29]

Another way to study the relation between the electronic states and the conductance in low-dimensional systems is through conductance graphics as a function of the total energy and magnetic field. In a QW a "three-dimensional butterfly" is observed.[30] This representation summarizes a number of well-known facts about magnetotransport with the quasi-Landau levels defining the conductance plateaus frontiers. The projection of the conductance in the energy-magnetic field plane result in the Hofstadter butterfly.[31] If an antidot lattice is now considered inside the QW region, the electrostatic confinement potential of the antidots generate a discretization of the available quasi-Landau bands (conductance plateaus in the three-dimensional butterfly). It occurs because in this situation, the discrete states associated with the OQDs induced by the antidot lattice govern the electronic quantum transport through the system.[32]

On the other hand, not much attention was given to the relationship between the crossover and closing of the induced electronic states with the magnetoconductance intensity variation, which can give useful information about the longitudinal and transverse transport through the system. This is very important if we want to understand, for example, the regime of quantum Hall effect. The purpose of this paper is to discuss the longitudinal and transverse couplings between the electronic states of the system (associated with the induced OQDs) when we vary the antidot lattice potential and the QPCs width that connected to reservoirs in the presence of an applied magnetic field. Also, it is important to be able to identified these transverse couplings in the longitudinal conductance maps. We suggest along the work some transverse coupling fingerprints that can be directly observed from the experimental data. As a consequence of the systematic analysis performed in this work, we have observed a non

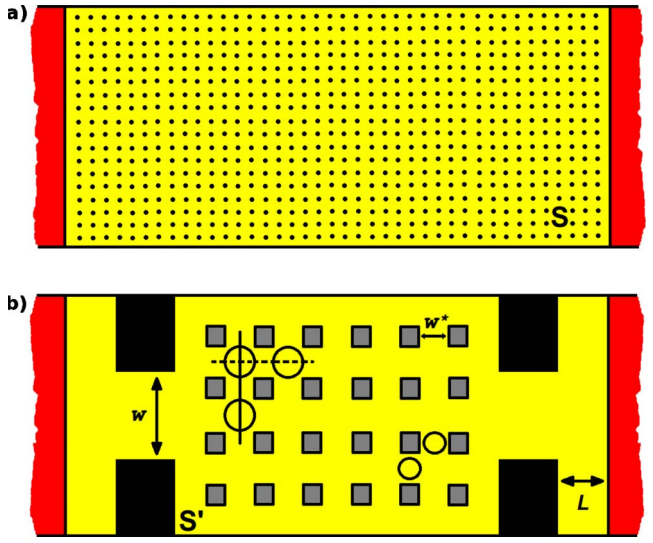

FIG. 1. (Color online) (a) Schematic of the system. In yellow the quantum wire region S with a discretization (dots) of 80×200 tight-binding sites. In red the left and right reservoirs. The magnetic field perpendicular to the plane is uniformly applied over S. (b) The rectangular region S' (central part) with an antidot lattice is located over the region S and coupled to the reservoirs using QPCs of variable with w. The antidot lattice-induced OQDs (big circles) and QPCs (small circles). The black squares refer to regions with high potential barriers.

expected continuous channel in our conduction maps simulations, this one being responsible for the generation of Fano resonances in the magnetoconductance. These results bring interesting lights in the study of electronic magnetotransport through antidot lattices.

This work is organized as follows, in the next section we introduce the system of antidot lattice together with a brief overview of the mathematical method used in our simulations. In Sec. III, we analyzed the antidot lattice effects over the conductance maps of the system. We focus basically in two phenomena, the closing and crossover of states and the transverse and longitudinal couplings between the induced OQDs of the system. In Sec. IV, we continue our analysis by considering the effects of the QPCs widths variation in the conductance maps profile of our system. Finally, in Sec. V, a summary of our results concludes the work.

II. MODEL

We start our model considering a two-dimensional discretization of a QW. The QW region S has a 80×200 tight-binding lattice sites with an uniform magnetic field applied perpendicular to the QW plane, Fig. 1(a). The tight-binding lattice represents the discretization of the continuous behavior of the envelope wave function of the electrons in the two-dimensional electron gas. To verify if the considered discretization is suitable for studying the mesoscopic effects of our work, we have also experienced with smaller (60×170 tight-binding sites) and bigger (100×230 tight-binding sites) lattices and we obtained similar results. In Fig. 1(b), an antidot lattice of area S' (covering 80×120 tight-binding sites) is built inside the region S. Each antidot has the following features: (i) a sharp square shape with size equal to $6a\times6a$, with $a=20$ Å being the discretization parameter used in our tight-binding lattice and (ii) a potential height V_a variable from 0 to 0.5 eV. This simple system contains all the necessary elements (induced OQDs and QPCs) to study the interference effects that generates crossovers and closings of the induced OQDs states as a function of the applied magnetic field. The region S' (containing the antidot lattice) is attached to the electron reservoirs at each side using QPCs connectors of variable width w, $20a<w<80a$. In Fig. 1(b), a 6×4 square antidot lattice is considered inside the OQD. Inside the OQD region, the antidots generate smaller OQDs that can be transversally coupled (continuous lines) or longitudinally coupled (dashed lines) by the induced QPCs (small circles). The width of the induced QPCs is the distance (transverse or longitudinal) between the antidots, i.e., $w^*=14a$. Under these conditions, the quantum transport through the system is controlled by the coupling between the induced OQDs, the continuous bands of the induced QPCs, the electronic states related to the reservoirs QPCs of width w, and the applied magnetic field that modulates the couplings between the electronic states of the induced OQDs and QPCs.

In order to test our numerical code, we have calculated a longitudinal conductance map, i.e., longitudinal conductance vs energy of incident electrons vs applied magnetic flux, of a system with $V_a=0$ eV and $w=80a$ (a straight QW without antidot lattice). The results are presented in Fig. 2(a). In this figure, the lighter (darker) region corresponds to the maximum (minimum) conductance of $5\times2e^2/h$ (0). At each plateau, the conductance rises $2e^2/h$. In the inset of Fig. 2(a), a conductance map shows the typical behavior of the host tight-binding lattice, a Hofstadter butterfly. In this work, we are interested in the limit of low energies ($E<7$ meV) and low magnetic fluxes ($\phi/\phi_0<1\times10^{-3}$, $\phi_0=h/e$, $\phi=Ba^2$). In Fig. 2(a), we can clearly see the quasi-Landau levels being perturbed by the transverse confinement of the QW. For low magnetic fluxes, the conductance map curve differs from their typical linear behavior, see, for example, the first and second quasi-Landau level for $\phi/\phi_0<0.5\times10^{-3}$. For larger fluxes, the linear behavior of the firsts Landau levels is recovered. This can be observed using a smaller scale in the inset of Fig. 2(a) for $1\times10^{-3}<\phi/\phi_0<0.05$, not shown here.

Note that a discontinuity in the potential between the region S and the leads is produced due to the magnetic field present only in S. This discontinuity was took into account in our numerical simulations. However, in the limit of low energies and low applied magnetic fields considered in this work, the quantum confinement in the system is mostly governed by the QPCs electrostatic potentials and the antidot lattice rather than the magnetic field. This will be seen through the paper in the relation between the geometry of the electrostatic confinement and the number of transverse band and longitudinal states. The spurious effects caused by the magnetic step inside our system were also minimized by considering a suitable length L between the QPC and the semi-infinite leads without compromising the computational time cost. For this work, we consider L equal to 20 tight-binding discretization sites.

The method used in our simulations consists of a hybridization between the self-energy technique[33,34] and the recur-

sive Green's function method.[35–37] In the first part of the method, the total Hamiltonian of the system H_T (the region S) is written as a function of the Hamiltonians H_{mm} of each transverse chain in which the system is divided, together with the self-energies Σ^L and Σ^R to include the effects of the left and right leads on the cavity. We consider a system composed by $M(m=1,2,\ldots,M)$ transverse chains with N sites each $(p=1,2,\ldots,N)$. The magnetic field is included by means of a Peierls substitution using the Landau gauge, which is a common procedure in literature.[25,38] The total Hamiltonian in the subspace given by m can be written as

$$H_T = \begin{pmatrix} H_{11}+\Sigma^L & V_x & 0 & 0 & . & . \\ V_x & H_{22} & V_x & 0 & . & . \\ 0 & V_x & H_{33} & V_x & 0 & . \\ . & . & . & . & . & . \\ . & . & . & . & . & . \\ . & . & . & . & . & H_{MM}+\Sigma^R \end{pmatrix} \tag{2.1}$$

in which the longitudinal hopping submatrices V_x and the transverse chain Hamiltonian H_{mm} are expressed in the subspace p. In this representation, the submatrices V_x are diagonal with elements given by $\langle p|V_x|p\rangle = v_x = -\hbar^2/(2m^*a^2)$ with m^* being the effective mass. The self-energies are expressed as $\Sigma^L(E) = V_x^\dagger g_L(E) V_x$ and $\Sigma^R(E) = V_x^\dagger g_R(E) V_x$, where g_L and g_R are the Green's functions for the isolated lead contacts given by $(E-H_L)g_L(E) = \mathbf{I}$ and $(E-H_R)g_R(E) = \mathbf{I}$, with E the energy of the incident electrons, H_L (H_R) the Hamiltonian of the semi-infinite left (right) lead and $\mathbf{I}$ the unitary matrix. Explicit expressions for g_L and g_R are shown in Ref. 33. Each transverse chain Hamiltonian H_{mm} is described by

$$H_{mm} = H_m(B) = \begin{pmatrix} \epsilon_1^m & v_y & 0 & 0 & . & . \\ v_y & \epsilon_2^m & v_y & 0 & . & . \\ 0 & v_y & \epsilon_3^m & v_y & 0 & . \\ . & . & . & . & . & . \\ . & . & . & . & . & . \\ . & . & . & . & . & \epsilon_N^m \end{pmatrix}, \tag{2.2}$$

where $\epsilon_p^m = 2\hbar^2/(m^*a^2)$ is the site energy. The transverse hooping energies v_y using the Landau gauge $\mathbf{A} = (0, -Bx, 0)$ become[25]

$$v_y = |v_x| \exp(i 2\pi p \phi/\phi_0). \tag{2.3}$$

The above representation allow us the use of conventional recursive Green's function methods for calculating the transmission probabilities through the system. This method has already been described throughout the literature and has been applied in a variety of problems in the context of mesoscopic systems.[36,37] For the sake of clarity, we briefly sketched it below.

To calculate the conductance through the system, we must construct from H_T the Green's functions G^T and G^R that are related to the transmission and reflexion amplitudes of the incident wave functions, respectively. This is accomplished by means of a recursive procedure based on the Dyson equation. This procedure unable us to successively couple the individual transversal chains in which the system was divided. Starting from the Dyson equation, we can obtain[36] two recursive numerical relations for the Green's functions G^R and G^T given by

$$G^T = G^T V_x (\mathbf{I} - G_j V_x G^R V_x)^{-1} G_j \tag{2.4}$$

and

$$G^R = (\mathbf{I} - G_j V_x G^R V_x)^{-1} G_j, \tag{2.5}$$

where $j = M-1$, $M-2,\ldots,1$, and G_j is the corresponding Green's function for an individual transverse chain obtained from

$$G_j(E,B) = [(E+i\eta)\mathbf{I} - H_j(B)]^{-1}, \tag{2.6}$$

when $\eta \to 0$.

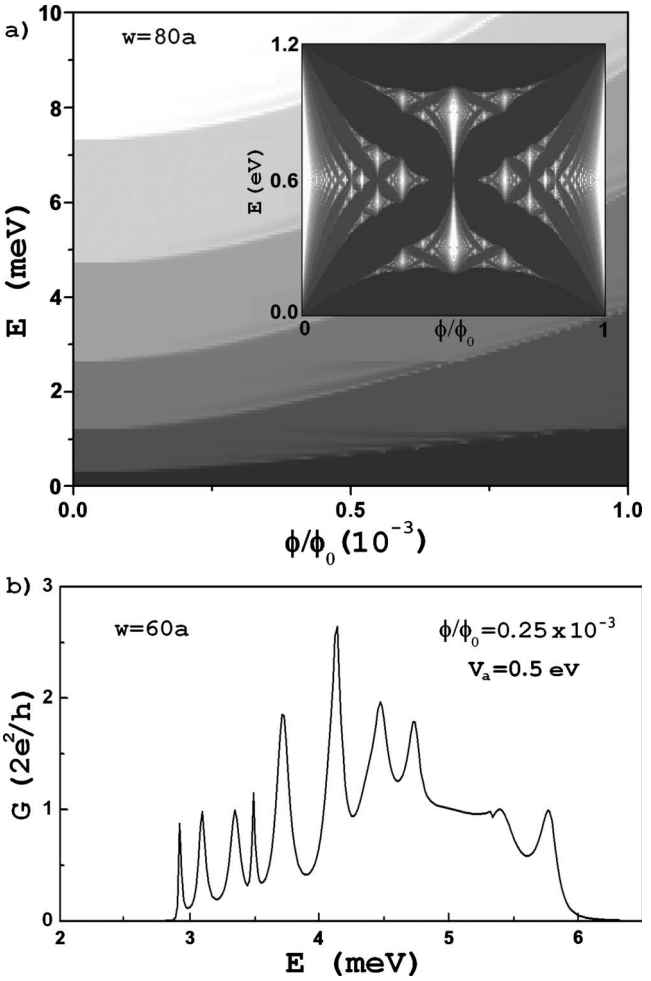

FIG. 2. (a) Longitudinal conductance map for a QW without antidot lattice and $w=80a$ (straight QW). We see the quasi-Landau levels being perturbed by the transverse confinement of the QW. In the inset, a conductance map shows the typical behavior of the host tight-binding lattice, a Hofstadter butterfly. (b) A typical longitudinal conductance profile. Different peaks in width and intensity are observed in the region of both low-energy and low applied magnetic flux.

The starting point of this iterative procedure is the coupling between the Green's function of Eq. (2.6) of the transversal chain at the right side of the structure, i.e., $r=m=M$, $G_M=[(E+i\eta)\mathbf{I}-H_M(B)-\Sigma^R(E)]^{-1}$, with the $j=M-1$ chain given by $G_{M-1}=[(E+i\eta)\mathbf{I}-H_{M-1}(B)]^{-1}$. Note that we have already included the contribution of the right semi-infinite lead inside G_M. As the starting condition for the iterative procedure, we have considered that $G^R=G^T=G_M$. Using the recursive relations of Eqs. (2.4) and (2.5), the function G_M can be coupled to the chain $j=M-1$ resulting in a new pair of functions $\{G^R,G^T\}$. These new functions can be used in the next iteration to couple the $j=M-2$ chain to the previous ones. Following this procedure all the individuals chains can be successively coupled to each other until we reach the transversal chain at the left contact, i.e., $l=j=1$ and $G_1=[(E+i\eta)\mathbf{I}-H_1(B)-\Sigma^L(E)]^{-1}$. Note that, as before, we have included the self-energy of the lead inside G_1.

After the recursive procedure is complete, the final Green's functions G^T and G^R can be used to calculate the transmitted and reflected amplitudes as

$$t_{\nu,\nu'}(E,B) = i2|v_x|\sqrt{\sin\theta_{\nu'}\sin\theta_\nu} \times \exp[i(\theta_\nu l - \theta_{\nu'} r)]G^T_{\nu,\nu'}(E,B) \quad (2.7)$$

and

$$r_{\nu,\nu'}(E,B) = i\sqrt{\frac{\sin\theta_{\nu'}}{\sin\theta_\nu}}\exp[i(\theta_\nu+\theta_{\nu'})l] \times (2|v_x|\sin\theta_\nu G^R_{\nu,\nu'}(E,B) + i\delta_{\nu,\nu'}) \quad (2.8)$$

with ν and ν' equal to the entrance and exit transverse mode, respectively, and $G^{R(T)}_{\nu,\nu'}=U^\dagger G^{R(T)}U$, with U being the unitary transformation from the sites to the transverse-mode representation. The function $\theta_{\nu(\nu')}$ is defined as

$$\theta_\nu = \cos^{-1}\left(\frac{E-E^\nu}{2v_x}+1\right) \quad (2.9)$$

with

$$E^\nu = 2v_x - 2v_x\cos\left(\frac{\pi\nu}{N+1}\right). \quad (2.10)$$

Finally the longitudinal conductance through the system is calculated using the Landauer-Büttiker formula given by

$$G(E,B) = \frac{2e^2}{h}\sum_{\nu'}^{N}\left(\sum_{\nu}^{N}|t_{\nu,\nu'}(E,B)|^2\right), \quad (2.11)$$

where the sum is performed considering all the available modes ν and ν' of the system. The number 2 in Eq. (2.11) accounts for the spin degeneracy.

In this work, we have simplified our system using a square lattice with sharp square antidots. The use of this simple model is justified because the qualitative effects that can be observed in real systems, for example, the relation between the conductance and the crossovers and closings of states induced by the applied magnetic field, do not change with the choose of a more realistic confinement potential (soft potential). In Fig. 2(b), we show a typical longitudinal conductance profile, $G(E)$, for a 6×4 antidot lattice with $w=60a$, $V_a=0.5$ eV, and $\phi/\phi_0=0.25\times10^{-3}$. Different peaks in width and intensity are present, together with a non expected plateau, forming a set of difficult interpretation. The purpose of the next sections is to analyze these peaks and plateaus and their relationship with the crossovers and closings of states observed in the longitudinal magnetoconductance maps.

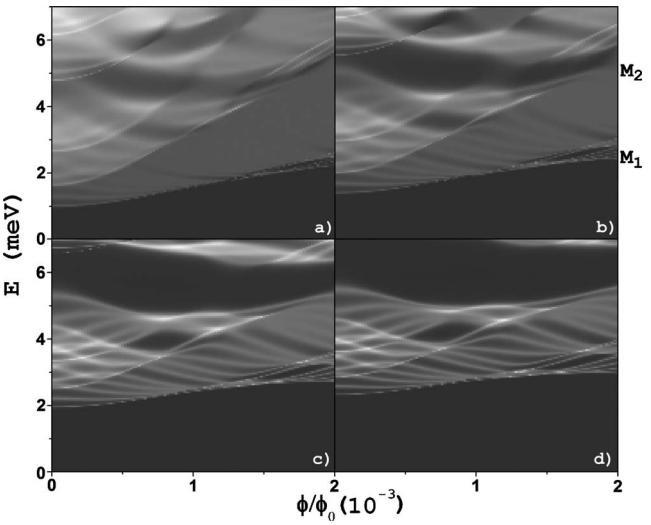

FIG. 3. Longitudinal conductance maps for different values of the antidot potential height V_a with $w=80a$ for the 6×4 antidot lattice system. We can follow the discretization of the conductance bands as we increased V_a: (a) 0.01 eV, (b) 0.02 eV, (c) 0.05 eV, and (d) 0.1 eV. The two lowest transverse bands M_1 and M_2 are still visible for potential heights up to 0.02 eV.

III. ANTIDOT LATTICE EFFECTS

A. Closing of states inside a band

We proceed to discuss the influence of the antidot potential height V_a in the conductance maps. In Figs. 3 and 4, we shown for $w=80a$ our numerical conductance maps simulations for several values of the antidots potential height, $0.01<V_a<0.5$ eV, and applied magnetic flux, $0<\phi/\phi_0<2\times10^{-3}$ ($0<B<2.1$ T). We can follow the evolution of the plateaus (bands associated with the quasi-Landau levels) previously shown in Fig. 2(a) to a set of discrete states. This discretization is produced by the quantization of the wave function in both transverse and longitudinal directions inside the induced OQDs of the system. A perturbative regime of $V_a=0.01$ eV is enough to modify the QW longitudinal magnetoconductance. Note from Fig. 3 that the discretization of the states are better defined as we increase V_a. Also, the continuous states related to the straight QW case of Fig. 2(a) are shifted to higher energies, and the discrete states induced by the OQDs began to interact with upper bands states. As we increased the antidot confinement potential V_a, the OQDs are more well defined and the induced QPCs create new continuous longitudinal channels with energy higher than that of the OQDs discrete ground states. In this way, the peaks that appear in the longitudinal conductance maps

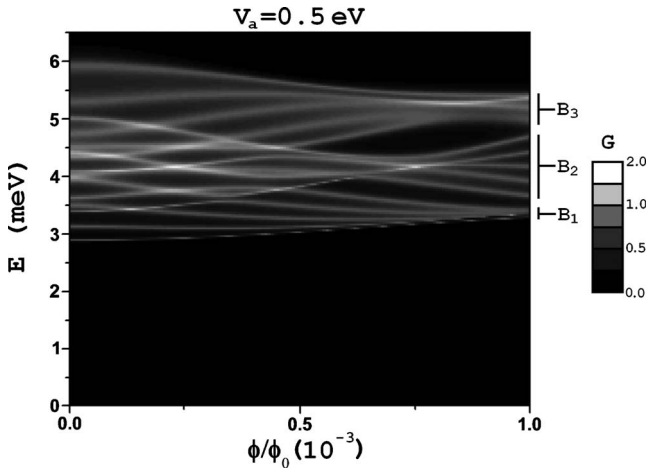

FIG. 4. Longitudinal conductance map for the 6×4 antidot lattice system with $w=80a$ and $V_a=0.5$ eV. The three transverse bands (each one containing five longitudinal modes) generated by the antidot lattice are indicated by B_1, B_2, and B_3. The brighter regions show points of high conductance due to the closing of longitudinal states and interband crossover.

(lighter regions) are the consequence of resonant tunneling through the quasibound states of the induced OQDs. Note also that the first transverse mode of the straight QW case of Fig. 2(a) is very robust and can be clearly seen even for potentials up to $V_a=0.1$ eV, see mode M_1 in Fig. 3. This is a feature of the QW transverse confinement in low applied magnetic fields.

In Fig. 4, we show the conductance map where crossover and closing of states are present. A direct comparison between Figs. 1(b) and 4 allows the identification of three bands (B_1, B_2, and B_3) related to the three vertically induced OQDs in the antidot system. Each one of these transverse bands has five states which are related to the five longitudinally induced OQDs of the system. In this context, the closing of states in a given transverse band can be interpreted as a longitudinal decoupling of the OQDs of the system. However, notice the existence of a finite longitudinal conductance greater than one quantum of conductance under this circumstance, and not a low conductance (less than or equal to one) due to the decoupling of the longitudinal OQDs. The high conductance situation could be explained (a) by a simple sum of longitudinal spatial channels (when the transverse spatial channels are uncoupled, as would happen with parallel QPCs (Ref. 39) isolated by a huge potential barrier) or (b) by a combination of transverse and longitudinal couplings[40] that could generate longitudinal transport. The last situation is likely to occur when potential barriers that uncouples the induced OQDs in the longitudinal direction are formed inside the system due to the applied magnetic field, forcing in this way transverse couplings. Since we have not observed an integer quantum of conductance ($n2e^2/h, n=2,3,\ldots$) in the longitudinal decoupling of our system (decrease in splitting), we can discard possibility (a). This will be further discussed in the next section.

B. Crossover of states of different bands

In order to discuss the importance of the transverse and longitudinal OQD couplings in the longitudinal conductance

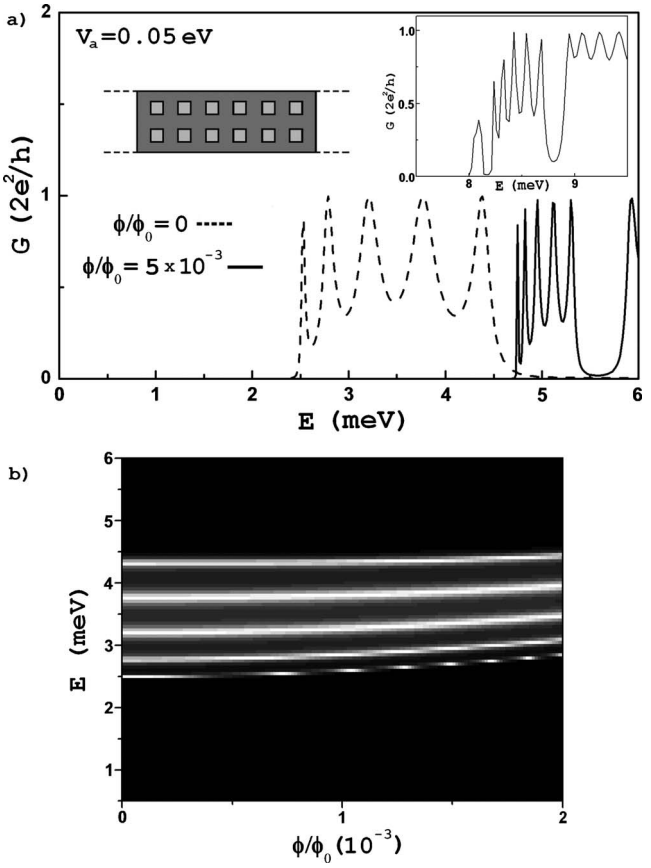

FIG. 5. (a) Conductance profile of the 6×2 antidot lattice system with $V_a=0.05$ eV for three values of magnetic flux ϕ/ϕ_0: 0 (dashed line), 5×10^{-3} (solid line), and 9×10^{-3} (inset curve). (b) Conductance map profile showing the five longitudinal states for fluxes up to 2×10^{-3}. Note the conductance quasilinear behavior of the system.

of the 6×4 antidot system [Fig. 1(b)], we start our analysis by considering more simpler systems, e.g., Figs. 5 and 6. The system shown in the inset of Fig. 5(a), a 6×2 antidot lattice, does not generate transverse coupling since it is a purely longitudinal system. We can observed in Fig. 5(a) five bound states related to the five induced longitudinal OQDs for three applied magnetic fluxes: 0; 5×10^{-3} and 9×10^{-3} (inset). Note that longitudinal states of different bands do not couples even for high magnetic fields (>2.1 T or $\phi/\phi_0 > 2\times10^{-3}$), and their conductances do not exceed a quantum of conductance. This case is similar to the one of a single OQD without transverse coupling in which the conductance of the system, even when crossovers of longitudinal states occurs, do not generate conductance intensities greater than one quantum of conductance. This fact could represent a fingerprint of purely longitudinal coupling. Figure 5(b) shows that the conductance map for the 6×2 system has a quasilinear behavior for all states in applied magnetic fluxes up to 2×10^{-3}, without any presence of crossing and closing of states. We will see below that this is related to the absence of transverse coupling.

In Fig. 6(a), we show the conductance profile of the 6×3 antidot lattice system for two values of applied magnetic flux ϕ/ϕ_0: 0 ($B=0$ T) and 1×10^{-3} ($B=1$ T). Intensities

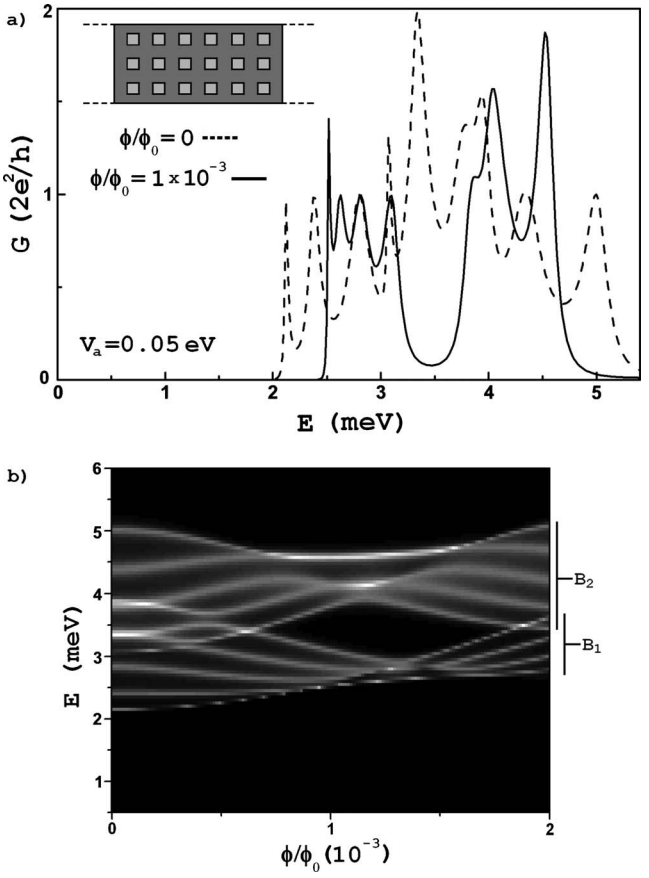

FIG. 6. (a) Conductance profile of the 6×3 antidot lattice system with $V_a=0.05$ eV for two different values of applied magnetic flux ϕ/ϕ_0: 0 (dashed line) and 1×10^{-3} (solid line). Intensities larger than one quantum of conductance appear as a consequence of transverse couplings. (b) Conductance map profile showing the two transverse B_1 and B_2 bands with five longitudinal states each for magnetic fluxes up to 2×10^{-3}. The crossing and closing of the bands occurs at certain values of the applied magnetic field.

greater than one and less than two quantum of conductance are observed in both cases. In Fig. 6(b), we see that for certain values of applied magnetic field, it is possible to distinguished two bands, B_1 and B_2 with five longitudinal states each, generated by the induced transverse OQDs of the system. In some regions, the longitudinal states of the two bands suffer couplings between transverse bands generating higher conductance intensities (lighter regions). This fact can be interpreted as a fingerprint of transverse coupling between the induced OQDs.

In general, an increase in the conductance is observed in two situations: (a) when some of the longitudinal states inside a band couples with states of different transverse bands (crossovers) and (b) when the longitudinal states uncouples (closing of the band). A direct comparison between Fig. 5 and 6 allows us to relate all the previous situations to the transverse couplings between induced OQDs. We expect in case (b) a decreased in the conductance $[G(E)\leq1]$, however we observed in our calculations an enhancement in $G(E)$. This fact indicates that the transport is favored by the opening of spatial transverse channels. We can see from the center peak of Fig. 6(a), for $\phi/\phi_0=0$, that a simple sum of spatial channels will double the conductance, which is typical in systems with degenerate states. This happens as a consequence of the sum of two longitudinal states of different uncoupled transverse bands for the given energy and magnetic field ($B=0$ T). After the magnetic field is applied, another crossover between the same states occurs. In this situation, the magnetic field couples the induced OQDs of the system as we have $1<G(E)<2$ quantum of conductance. Anticrossovers are also observed between states of different bands for other values of the applied magnetic field and energy [see, for instance, Fig. 6(b) at $\phi/\phi_0\sim0.42\times10^{-3}$ and $E\approx3.5$ meV]. The intensity here is one quantum of conductance for each state. We interpret this behavior as a longitudinal couplings between the induced OQDs.

We have not observed, after the application of a magnetic field, conductances equal to or greater than two quantum of conductance in our simulations of the 6×3 antidot lattice system. Nevertheless, the transverse interference effects modulated by the magnetic field are responsible for the enhancement of the conductance in the closing and crossover regions. In the extreme case of high magnetic fields, we expect that the transport through the system to be controlled by the magnetic border states.

Finally, we see from Fig. 6(b) that the two higher energy states of the upper band suffer a closing and remain separated from the rest of the band. The conductance intensity in this situation is enhanced, as we can see from Fig. 6(a), by a transverse coupling that mixture longitudinal and transverse spatial channels in the antidot lattice. A similar situation is observed for the two lower energy states of the bottom band. Here again, the higher conductance can only be explained by transverse coupling between the induced OQDs.

We are now able, after the previous systematic analysis, to interpret the results of our original 6×4 antidot lattice system which are shown in Fig. 7(a) for $V_a=0.5$ eV, $w=80a$, and two values of applied magnetic field, $B=0$ T and $B=1$ T. The figure compares the conductance map of Fig. 4 with his conductance profile $G(E)$ for the given parameters. We emphasize the correspondence between the figures. In this system, we observed the definition of three transverse bands, i.e., B_1, B_2, and B_3. The central band B_2 at $B=1$ T clearly shows the five longitudinal states with intensities of one quantum of conductance each. This suggests that the states are pure longitudinal with no transverse couplings with the bands B_1 and B_3 (solid line). Each one of the other two bands, B_1 and B_3, present closing of the states (splitting decreased) and intensities higher that one quantum of conductance. This can be explained by a transverse coupling between the induced OQDs of the system. The fact that the high intensity is less than two quantum of conductance ensures the presence of interference effects, and indicates that the conductance is controlled by transverse transport channels of the induced OQDs.

To finalize, let emphasize that transverse coupling effects can also be obtained by modifying the antidot confinement potential height in the presence of a constant applied magnetic field. In Fig. 7(b), we show how the conductance profile of Fig. 7(a) is modified when we shift the potential height from 0.5 to 0.05 eV. Note that this action produces similar effects than the variation in the magnetic field, i.e.,

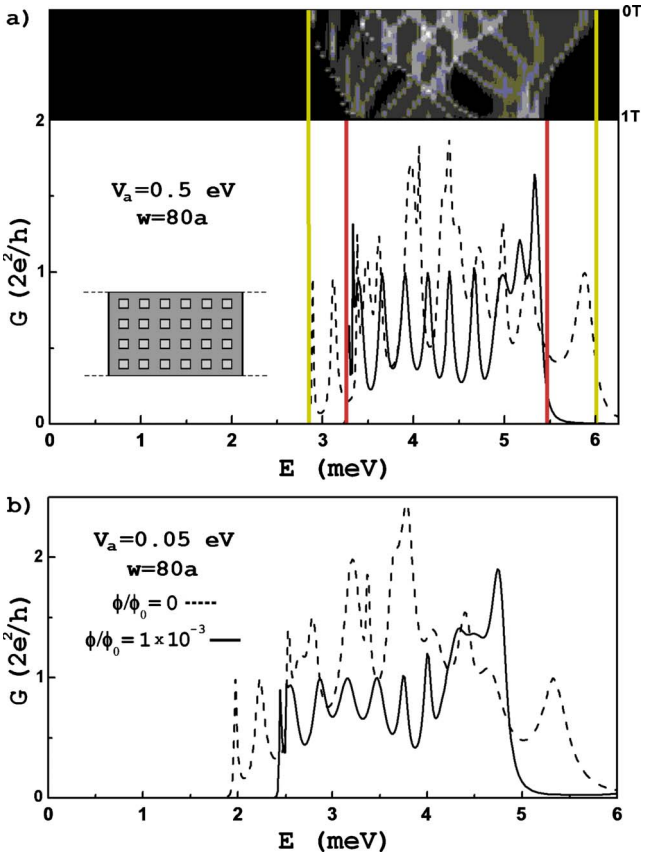

FIG. 7. (Color online) (a) (Color online) A comparison between the conductance map of Fig. 4 and the conductance profile $G(E)$ of a 6×4 antidot lattice for two applied magnetic field $B=0$ T (dashed line) and 1 T (solid line). We observed the correspondence between both figures delimited by the red ($B=1$ T) and green ($B=0$ T) lines. Three well-defined transverse bands appear in the system. (b) Conductance profile considering a low antidot potential height for $\phi/\phi_0=0$ (dashed line) and $\phi/\phi_0=1\times10^{-3}$ (solid line).

changes in the transverse couplings of the system. As an example, the higher energy state of the B_2 band couples with the B_3 band modifying its intensity to a value greater than one quantum of conductance.

IV. QUANTUM POINT-CONTACT EFFECTS

The effect of the QPCs width w variation [Fig. 1(b)] that connect the 6×4 antidot lattice with the reservoirs is discussed. In Fig. 8(a), we show our conductance map simulations for $w=80a$, $60a$, and $20a$. We observed in all cases the previously defined transverse bands B_1, B_2, and B_3. A nonexpected situation for the $w=60a$ case is observed, a broadening of the resonance lines of the upper band B_3. In the broadening region, the conductance intensity is approximately constant (one quantum of conductance) forming a conductance plateau B_{3c} allowing the system to behave as a QPC. This situation is shown in Fig. 8(b) for $\phi/\phi_0=0.25\times10^{-3}$ (dashed line) in the range from 5 to 6 meV. The role of the transverse couplings in the formation of the B_{3c} band will be discussed at the end of this section.

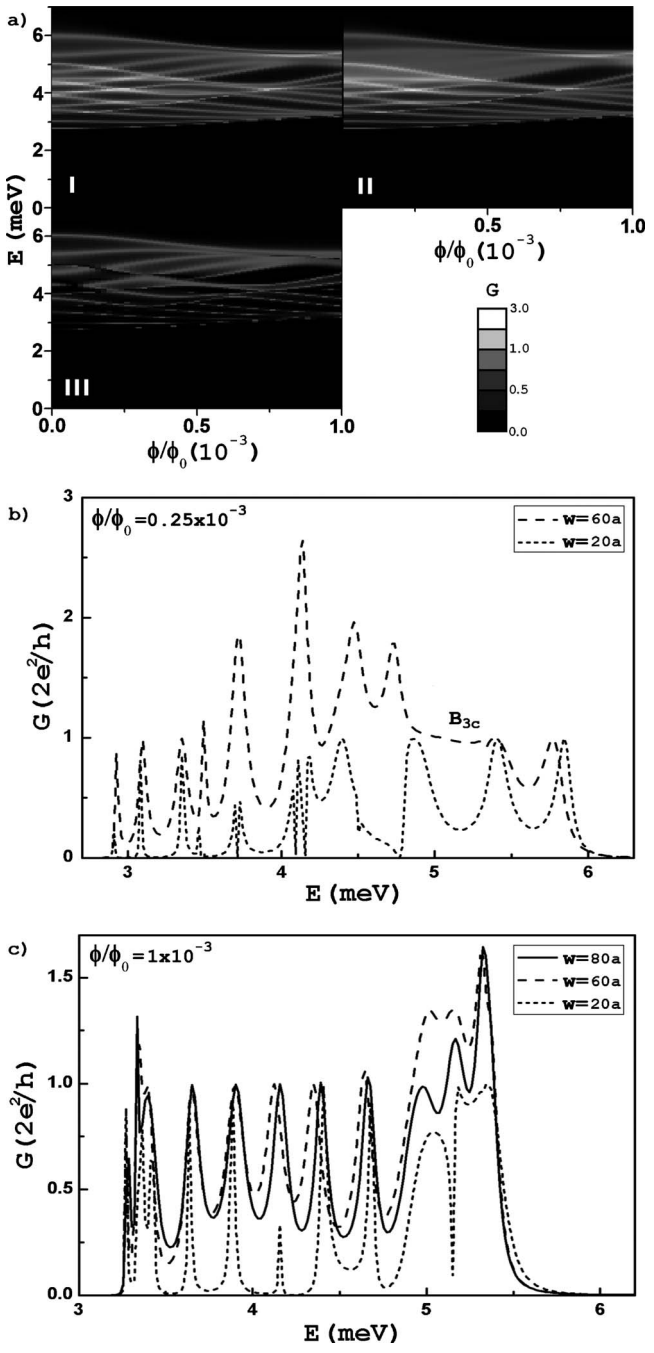

FIG. 8. (a) Conductance maps for $V_a=0.5$ eV and different values of the QPCs width w: (I) $80a$, (II) $60a$, and (III) $20a$. (b) Conductance profile at $\phi/\phi_0=0.25\times10^{-3}$ for two values of QPCs width. (c) Conductance profile at $\phi/\phi_0=1\times10^{-3}$ for several values of QPCs width.

As we decrease w from $80a$ to $60a$, we observed an increase in the conductance [see Fig. 8(c)] in the B_3 band at the closing region of Fig. 8(a)I and II for $\phi/\phi_0=1\times10^{-3}$. Similar behavior was observed in the crossover region at $\phi/\phi_0=0.25\times10^{-3}$. The enhancement of the conductance can be associated to the appearance of the induced continuous band B_{3c} that is added to the previously existed discrete channels. This can be seen in Fig. 8(a)II where a well-defined white line (higher energy state of the B_2 band) in the overlap region

with the continuous band B_{3c} does not present Fano resonances, clearly suggesting a channels sum. These processes, conductance enhancement and increase in the linewidth, are in contrast with those found in single OQDs for low energies or quantum billiards for high energies.

In Fig. 8(b), the decrease in the QPCs connectors to $w=20a$ generates Fano resonances and a decrease in the conductance at the crossover regions. The Fano resonances can be explained by the coupling between the continuous B_{3c} band and the available discrete states. In Figs. 8(b) and 8(c), we observed that in the regions in which $G(E)$ has a quantum of conductance for the $w=60a$ case, the decreasing to $w=20a$ creates thinner resonant lines, that is the expected response of the system. However, in the regions where the intensity was greater than one quantum of conductance, Fano resonances were observed. Note that these regions are the crossovers of Fig. 8(b) and the closings of Fig. 8(c), both related to transverse couplings. Moreover, Fig. 8(c) also presents what it seems to be a Fano resonance in the energy range of 5–5.5 meV. This resonance can not be explained in first approach by a continuous band since no continue band was observed in that region. However, in the forthcoming paragraph we will see that Fano resonances can occur even with a single conductance peak if its width grows sufficiently enough to behave like a continuous band. In general, transverse couplings are always generating high conductance intensities. For the low magnetic-flux situation, this can be understood as a crossing between different bands of longitudinal states or transverse couplings between induced OQDs. For the case when closing occurs, a qualitative explanation had been previously discussed in this work. In the $w=60a$ situation, the transverse coupling modulate the generation of the continuous B_{3c} band that are favored by the specific position of the QPCs connectors. Other QPCs configurations can, in principle, induce the formation of new continuous bands B_{1c} or B_{2c}.

To verify the above ideas and the existence of the continuous band B_{3c} and their relationship with the transverse couplings, we will use Fig. 9. In this figure, we consider a 2×4 antidot lattice system that only support transverse couplings between the induced OQDs (inset of figure). We observe that for $w=80a$ and without magnetic field (black line), a splitting in the conductance profile related to the three induced OQDs appears, each one associated to the B_1, B_2, and B_3 bands previously seen in Fig. 7(a) at $\phi/\phi_0=1\times10^{-3}$. The transverse coupling between the induced OQDs generates a conductance intensity greater than one quantum, contrary to the case of Fig. 5(a) when we consider purely longitudinal couplings. This important fact gives us a clear fingerprint of transverse coupling.

Figure 9 shows that an applied magnetic field of $B=1$ T and $80a$ (blue line, the second one from top to bottom at 3 meV) generates a decrease in the conductance intensity, nevertheless we still have conductance intensities greater than one quantum of conductance, a manifestation of pure transverse coupling. We continue the system analysis by decreasing the QPC to $w=20a$ in the presence of the applied magnetic field (red line). Three major effects were observed after this process: (i) reduction in the linewidth for the two first peaks, (ii) Fano resonance at the center region, and (iii)

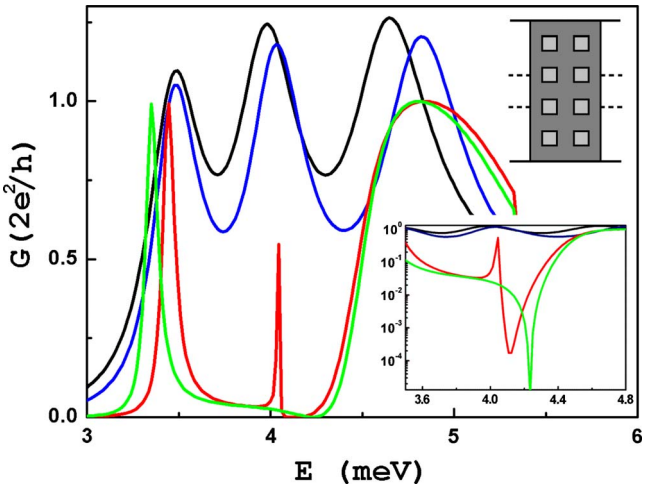

FIG. 9. (Color online) Conductance profile for a 2×4 system with $V_a=0.5$ eV in which transverse couplings are the only ones supported. Different configurations were tested: without magnetic field and $w=80a$ (black line), with an applied magnetic field of $B=1$ T and $w=80a$ (blue line), with an applied magnetic field of $B=1$ T and $w=20a$ (red line) and without magnetic field and $w=20a$ (green line). In the inset, we show in logarithmic scale the formation of an asymmetric Fano resonance (red line), and the formation of a pronounce dip (green line). The last one being a typical manifestation of transverse uncoupling in the system.

increase in the linewidth of the higher state. Note the importance of the third case which is responsible for the formation of the continuous band B_{3c} discussed before. The higher state couples with the central state generating an asymmetric Fano resonance (inset of figure). Finally, when the magnetic field is suppressed (green line), the central state disappears and form a pronounce dip (inset of figure) that indicates a transverse uncoupling with the others OQDs of the system. In general, the QPCs localization can be used to manipulate the transverse couplings inside the system (with a possible permutation of the effects between the states) with the help of an applied magnetic field. In this sense, the closing regions of the bands intrinsically support continuous channels that can be coupled to discrete states, generating in this way the Fano resonances. This gives a reasonable explanation for the Fano resonances found at the closing region of the B_3 band in Fig. 8(c).

V. CONCLUSIONS

In summary, we have discussed the evolution and handling of crossovers and closings of states observed in longitudinal conductance maps of a antidot lattice within a OQD when the antidots potential and the QPCs connectors width are modified. A systematic study of the relationship between the intensity of the longitudinal conductance and the crossovers and closings of the magnetic states leads to the determination of transverse couplings between the OQDs induced by the lattice. These transverse channels, modulated by the magnetic field, can contribute greatly to the longitudinal transport through the system.

In systems that can provide transverse couplings, the conductance map will not be linear and the conductance maps show transverse bands of longitudinal states, each band related to a transverse induced OQD in the system. At the closing and crossover regions, the intensities in our conductance maps present noninteger quantum values (but greater than one) of conductance. This indicates a coupling between states and not a simple sum of noncoupled channels. We can generate this coupling by inducing transverse OQDs in the system.

We have identified the closing of the bands as a fingerprint of decoupling between longitudinal states of a given band and the high intensities as transverse coupling between the induced OQDs. This conductance maximum can be used as a valuable fingerprint of transverse couplings, which can serve to control the electronic transport properties. This effect can be clearly observed and measured in experiments concerning $G(E,B)$.

Our results could also be observed in typical experiments with hundreds of electrons participating in transport. In this situation, the perturbative mean-field effect overcome the electron-electron interaction favoring the single-particle picture.[41,42] However, the Coulomb interaction in low electron-density regime can introduce another fingerprints in the magnetoconductance.[43,44] In this situation, the modulation of the QPCs connectors width would play an important role. Further research in this direction are necessary.

The effects of the transverse coupling in our system can be manipulated by the applied magnetic field, the antidot potential height and the QPCs connectors position and width. Changing the connectors width and positions, we were able to create a new continuous band or plateau inside a transverse band that generates Fano resonances. Also, we managed to fully uncouple a OQD for the rest of the system. This effect can be used, in principle, to selectively uncouple one OQD to control the electronic transport through the system. Note that the effects reported in this work can be observed in samples in which the antidot lattice is built in a regular way. If the antidots potential heights are different, the interference effects between the available electronic state could perturbed some of the features reported in this work, nevertheless the conductance maps will be qualitatively similar. We think that this work improves our understanding of electronic transport through antidots lattices.

ACKNOWLEDGMENTS

We acknowledge financial support from the "Fundação de Amparo à Pesquisa do Estado de São Paulo—FAPESP" and "Universidade Federal do ABC-UFABC." The authors thank P. A. Schulz for useful discussions.

*sebastian.ujevic@gmail.com

[1] K. v. Klitzing, G. Dorda, and M. Pepper, Phys. Rev. Lett. **45**, 494 (1980).
[2] C. Albrecht, J. H. Smet, K. von Klitzing, D. Weiss, V. Umansky, and H. Schweizer, Phys. Rev. Lett. **86**, 147 (2001).
[3] B. J. van Wees, H. van Houten, C. W. J. Beenakker, J. G. Williamson, L. P. Kouwenhoven, D. van der Marel, and C. T. Foxon, Phys. Rev. Lett. **60**, 848 (1988).
[4] M. A. Topinka, B. J. LeRoy, S. E. J. Shaw, E. J. Heller, R. M. Westervelt, K. D. Maranowski, and A. C. Gossard, Science **289**, 2323 (2000).
[5] A. Barelli, J. Bellissard, and F. Claro, Phys. Rev. Lett. **83**, 5082 (1999).
[6] K. R. Zolleis, C. J. B. Ford, B. Kardynal, D. A. Ritchie, E. H. Linfield, P. D. Rose, and G. A. C. Jones, Phys. Rev. Lett. **89**, 146803 (2002).
[7] J. P. Bird, *Electron Transport in Quantum Dots* (Kluwer Academic, London, 2003), p. 216.
[8] R. Nötzel, N. N. Ledentsov, L. Däweritz, K. Ploog, and M. Hohenstein, Phys. Rev. B **45**, 3507 (1992).
[9] H. Bässler, Nat. Phys. **2**, 15 (2006).
[10] K. Torfason, C. S. Tang, and V. Gudmundsson, Phys. Rev. B **80**, 195322 (2009).
[11] A. H. Aly and C. K. Hwangbo, Int. J. Thermophys. **30**, 661 (2009).
[12] J. Göres, D. Goldhaber-Gordon, S. Heemeyer, M. A. Kastner, H. Shtrikman, D. Mahalu, and U. Meirav, Phys. Rev. B **62**, 2188 (2000).
[13] A. Cresti, Nanotechnology **18**, 055403 (2007).
[14] A. Dorn, E. Bieri, T. Ihn, K. Ensslin, D. D. Driscoll, and A. C. Gossard, Phys. Rev. B **71**, 035343 (2005).
[15] H. Chen, J. J. Heremans, J. A. Peters, N. Goel, S. J. Chung, and M. B. Santos, Appl. Phys. Lett. **84**, 5380 (2004).
[16] I. V. Zozoulenko, F. A. Maao, and E. H. Hauge, Phys. Rev. B **56**, 4710 (1997).
[17] T. Ando, S. Uryu, and S. Ishizaka, Jpn. J. Appl. Phys. **38**, 308 (1999).
[18] J. P. Keating, S. D. Prado, and M. Sieber, Phys. Rev. B **72**, 245334 (2005).
[19] Y. Takagaki and K. H. Ploog, Phys. Rev. B **67**, 195323 (2003).
[20] R. Akis, D. K. Ferry, and J. P. Bird, Phys. Rev. Lett. **79**, 123 (1997).
[21] M. Mendoza and P. A. Schulz, Phys. Rev. B **74**, 035304 (2006).
[22] M. Mendoza, P. A. Schulz, R. O. Vallejos, and C. H. Lewenkopf, Phys. Rev. B **77**, 155307 (2008).
[23] S. Uryu and T. Ando, Phys. Rev. B **58**, 10583 (1998).
[24] M. C. Geisler, J. H. Smet, V. Umansky, K. von Klitzing, B. Naundorf, R. Ketzmerick, and H. Schweizer, Phys. Rev. Lett. **92**, 256801 (2004).
[25] P. H. Rivera, M. A. Andrade Neto, P. A. Schulz, and N. Studart, Phys. Rev. B **64**, 035313 (2001).
[26] P. Vavassori, G. Gubbiotti, G. Zangari, C. T. Yu, H. Yin, H. Jiang, and G. J. Mankey, J. Appl. Phys. **91**, 7992 (2002).
[27] S. Meckler, T. Heinzel, A. Cavanna, G. Faini, U. Gennser, and D. Mailly, Phys. Rev. B **72**, 035319 (2005).
[28] Y. Iye, M. Ueki, A. Endo, and S. Katsumoto, J. Phys. Soc. Jpn. **73**, 3370 (2004).
[29] B. L. Johnson, P. B. Kohl, and D. M. Retzlaff, Phys. Rev. B **66**,

153311 (2002).
[30] J. Skjånes, E. H. Hauge, and G. Schön, Phys. Rev. B **50**, 8636 (1994).
[31] D. R. Hofstadter, Phys. Rev. B **14**, 2239 (1976).
[32] J. P. Bird, R. Akis, and D. K. Ferry, Phys. Rev. B **60**, 13676 (1999).
[33] S. Datta, Superlattices Microstruct. **28**, 253 (2000).
[34] M. Mendoza and P. A. Schulz, Braz. J. Phys. **36**, 423 (2006).
[35] H. U. Baranger, D. P. DiVincenzo, R. A. Jalabert, and A. D. Stone, Phys. Rev. B **44**, 10637 (1991).
[36] D. Ferry and S. M. Goodnick, *Transport in Nanostructures* (Cambridge University Press, Cambridge, 1997).
[37] M. Mendoza and P. A. Schulz, Phys. Rev. B **68**, 205302 (2003).
[38] R. Peierls, Z. Phys. **80**, 763 (1933).
[39] E. Castaño and G. Kirczenow, Phys. Rev. B **41**, 5055 (1990).
[40] Y. Takagaki and K. Ploog, Phys. Rev. B **49**, 1782 (1994).
[41] T. Lundberg, J. E. F. Frost, K. F. Berggren, Z. L. Ji, C. T. Liang, I. M. Castleton, D. A. Ritchie, and M. Pepper, Semicond. Sci. Technol. **12**, 875 (1997).
[42] J. P. Bird, R. Akis, D. K. Ferry, D. Vasileska, J. Cooper, Y. Aoyagi, and T. Sugano, Phys. Rev. Lett. **82**, 4691 (1999).
[43] V. Gudmundsson and R. R. Gerhardts, Phys. Rev. B **52**, 16744 (1995).
[44] V. Gudmundsson and R. R. Gerhardts, Phys. Rev. B **54**, R5223 (1996).